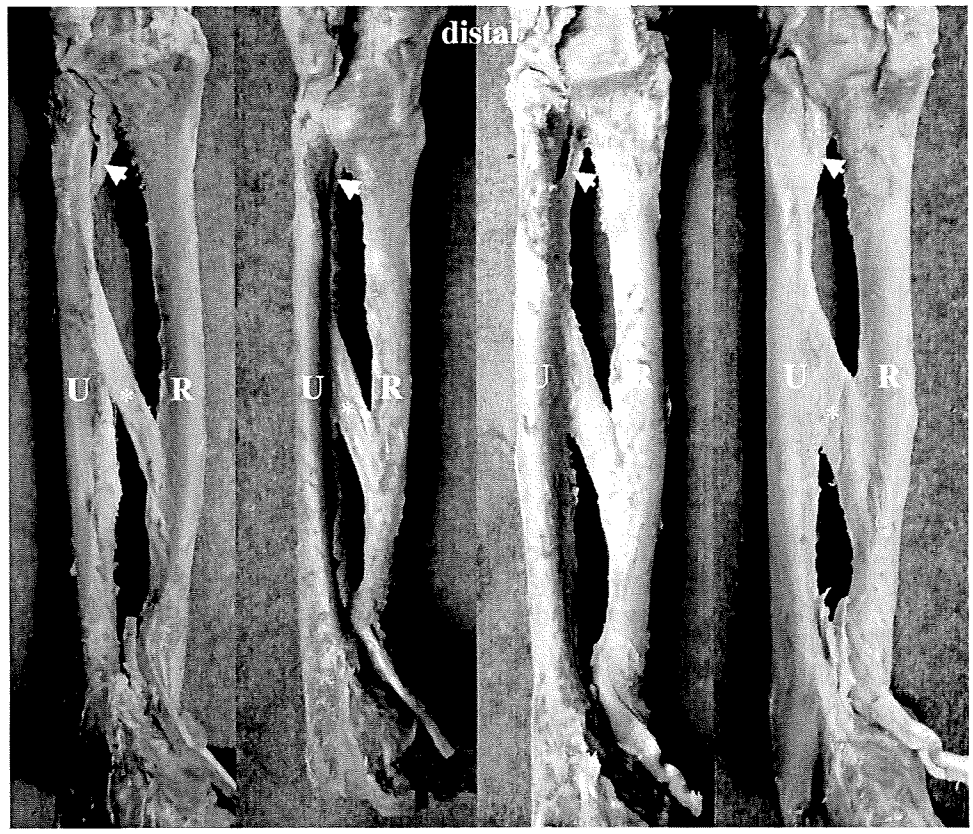


**FIGURE 4:** The CB and DOB, Four different right forearms are shown. Asterisks indicate the CB, and arrows indicate the DOB. The other ligamentous components were dissected. The CB is the thickest ligament and has a broad attachment. It originates from the interosseous crest of the radius, then courses distally and ulnarly and inserts into the interosseous border of the ulna. The CB was seen in all specimens.

fibers. The structure was less substantial (< 1 mm in thickness) and varied in location and number (Fig. 5). The AB was usually located distal to the CB, and the most distal ligament of the AB tended to be the stoutest of the AB fibers. In comparison, fibers were often absent proximal to the CB, and even if present, they were short and delicate. Of 30 specimens examined, the region distal to the CB showed a single ligament in 14 specimens, 2 ligaments in 3 specimens, 3 ligaments in 8 specimens, 4 ligaments in 1 specimen, 5 ligaments in 1 specimen, and 0 ligaments in 3 specimens. Conversely, the region proximal to the CB showed 0 ligaments in 17 specimens, 2 ligaments in 7 specimens, 3 ligaments in 5 specimens, and 4 ligaments in 1 specimen.

We chose the distal ligament for attachment measurement because it was the only structure of all AB fibers that existed in a relatively constant and stout fashion. The attachment locations of the AB fibers are detailed in Table 1.

### Distal membranous portion

The distal membranous portion was on the distal side of the middle ligamentous complex, spanning between the radius and ulna under the region of the pronator quadratus muscle. A hole existed in that portion, through which the interosseous artery passed.

*Distal oblique bundle:* A relatively thick fiber ran within the distal membranous portion along the distal ulnar shaft in all specimens (see Figs. 2, 3). We named this bundle of fibers the distal oblique bundle (DOB). It existed in the same coronal plane as the CB and AB fibers. Although thickness varied widely among specimens, obvious fibers were seen in 12 of 30 specimens. The DOB originated from approximately the distal one-sixth area of the ulnar shaft, approximately coinciding with the proximal border of the pronator quadratus muscle, and ran distally toward the distal radioulnar joint (DRUJ; Fig. 6). The fibers blended into the capsular tissue of the DRUJ and eventually the DOB inserted to the inferior rim of the sigmoid notch of the

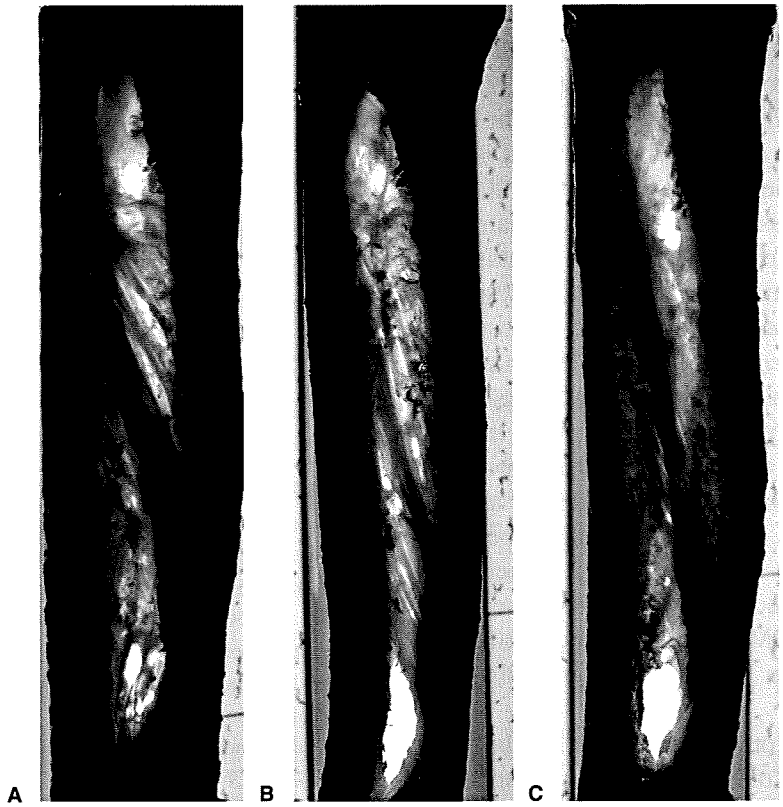


**FIGURE 5:** The AB. Three different right forearms are shown. Asterisks indicate the CB, and arrows indicate fibers of the AB. The fibers of the AB are less substantial than those of the CB. **A** Pattern of a few AB fibers distal to the CB, without any obvious fibers proximal to the CB. This pattern was seen often. **B** Pattern of AB fibers on either side of the CB. **C** Pattern with no obvious AB fibers on either side of the CB. R, radius; U, ulna.

radius. Furthermore, some fibers extended more distally along the anterior and posterior ridges of the sigmoid notch, so the DOB seemed to display continuity with the dorsal and palmar radioulnar ligaments of the triangular fibrocartilage complex (TFCC). The mean width was 4.4 ± 1.1 mm (range, 2–6 mm) and the mean thickness was 1.5 ± 0.5 mm (range, 0.5–2.6 mm).

The attachment locations of the DOB to the radius and ulna are listed in Table 1.

### Proximal membranous portion

The proximal membranous portion was on the proximal side of the middle ligamentous complex. The proximal membranous portion was overlaid by the origin of the flexor digitorum profundus muscle on the anterior aspect of the forearm and by the supinator muscle on the posterior aspect. A hole existed in that portion, through which the interosseous artery passed.

*Proximal oblique cord:* A ligament called the proximal oblique cord or ligament of Weitbrecht[12,17] was seen in the most proximal interosseous space (Fig. 7; see also Fig. 2) in all specimens. The proximal oblique cord originated from the anterolateral aspect of the coronoid process of the ulna (ulnar tuberosity) and inserted just distal to the radial tuberosity. The proximal oblique cord lay on the surface of the biceps tendon that attaches to the radial tuberosity. The mean width was 3.7 ± 1.6 mm (range, 1.5–8 mm) and the mean thickness was 1.1 ± 0.5 mm (range, 0.4–2 mm).

The sites of attachment of the proximal oblique cord to the radius and ulna are listed in Table 1.

*Dorsal oblique accessory cord:* A ligament called the dorsal oblique accessory cord was seen on the posterior aspect of the forearm (Fig. 8; see also Figs. 2, 3), located under the origin of the abductor pollicis longus muscle. The dorsal oblique accessory cord was found in 16 of 30 specimens. This ligament originated from around the distal two thirds of the ulnar shaft and inserted into the interosseous crest of the radius. The mean width was 3.2 ± 1 mm (range, 1.9–5 mm), and the mean thickness was 0.9 ± 0.2 mm (range, 0.5–1 mm).

The sites of attachment of the dorsal oblique accessory cord to the radius and ulna are reported in Table 1.

## DISCUSSION

Although past researchers have investigated the anatomy of the IOM,[1–7] to say that the history of IOM research is that of the CB is no exaggeration. The CB is frequently discussed in the literature because it is considered the most functional component of the IOM as the result of its stoutness and constancy. The name CB appears to have been first introduced by Hotchkiss and colleagues,[1] but the same formation was also described as the *intermediate descending fiber*[3]; the *cordlike portion*[4,6]; and the *tendinous part.*[5] Many cadaveric studies have been performed to investigate CB function.[1–3,8–11] They have revealed that the CB works as a restraint on the radius from proximal migration in cooperation with the radial head and the TFCC and also works as a load transmitter between the radius and ulna to redistribute load. Other studies[4,17–20] have indicated that the CB is an isometric component of the IOM and shows no change in tension during forearm rotation, thus providing stability to the forearm.

In comparison, the other components of the IOM have been described in only a few studies,[2–5] and their functions remain unclear. Skahen and colleagues[2] reported the AB and the proximal interosseous band, which corresponds to the dorsal oblique accessory cord in the present study. Poitevin[3] reported the proximal ascending bundle, which again corresponds to the dorsal oblique accessory cord in this study.

The functions of the AB have never been described in the literature. However, we suspect from the anatomical variations that function does not extend beyond a complementary nature, probably for the CB.

**TABLE 1. Attachment Locations of Interosseous Membrane Ligaments**

| | |
|---|---|
| CB | |
| Radial origin (distal end) | 53 ± 4% (46–61%) |
| Ulnar insertion (distal end) | 29 ± 4% (24–36%) |
| Radial origin (proximal end) | 64 ± 5% (51–74%) |
| Ulnar insertion (proximal end) | 44 ± 5% (34–52%) |
| Distal ligament of the accessory band | |
| Radial origin | 37 ± 5% (32–46%) |
| Ulnar insertion | 23 ± 3% (19–26%) |
| DOB | |
| Ulnar origin | 15 ± 2% (13–21%) |
| Radial insertion | 9.9 ± 0.8% (8.3–11%) |
| Proximal oblique cord | |
| Ulnar origin | 80 ± 2% (76–83%) |
| Radial insertion | 79 ± 2% (75–84%) |
| Dorsal oblique accessory cord | |
| Ulnar origin | 64 ± 9% (52–83%) |
| Radial insertion | 62 ± 3% (56–68%) |

Note: Based on 30 cadaveric forearms. Attachment locations are expressed as percentage of total bone length from the distal end. All data are represented as mean ± SD (range).

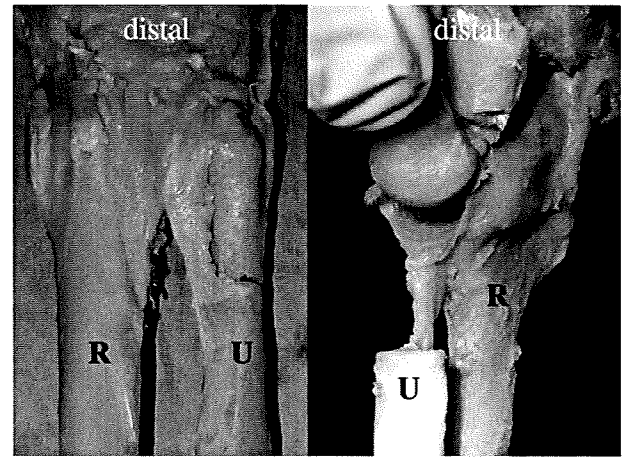


**FIGURE 6:** The DOB. The photograph on the left shows the DOB as seen from the dorsal aspect of the right forearm. This bundle originates from around the distal one sixth of the ulnar shaft and runs toward the DRUJ. The photograph on the right shows the DOB as seen from the ulnopalmar aspect of the same specimen. The ulna is cut just distal to the ulnar origin of the DOB and retracted distally. The DOB blends into the capsular tissue, through which it inserts into the inferior rim of the sigmoid notch of the radius. R, radius; U, ulna.

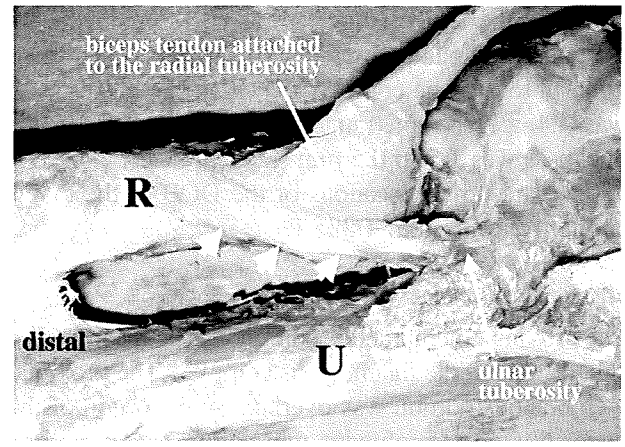


**FIGURE 7:** The proximal oblique cord. The right proximal forearm as seen from the anteromedial aspect. Arrows indicate the proximal oblique cord, originating from the anterolateral aspect of the coronoid process of the ulna (ulnar tuberosity) and inserting just distal to the radial tuberosity. The proximal oblique cord lies on the surface of the biceps tendon, which is attached to the radial tuberosity. R, radius; U, ulna.

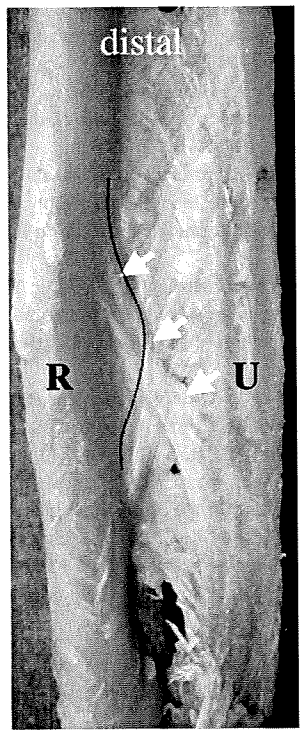


**FIGURE 8:** The dorsal oblique accessory cord. The right forearm viewed from the dorsal aspect. Arrows indicate the dorsal oblique accessory cord. The dorsal oblique accessory cord exists exclusively on the posterior aspect of the forearm, located under the region of origin of the abductor pollicis longus muscle. The cord originates from around the distal two thirds of the ulnar shaft and inserts into the interosseous crest of the radius (broken line). The dorsal oblique accessory cord was seen in 16 of 30 specimens. R, radius; U, ulna.

We identified the DOB, which was located within the distal membranous portion. Originating from around the distal one sixth of the ulnar shaft and running along the distal ulnar shaft toward the DRUJ, the DOB inserts into the inferior rim of the sigmoid notch of the radius. Furthermore, the DOB seems to exhibit continuity with the dorsal and palmar radioulnar ligaments of the TFCC. Watanabe and colleagues[21] insisted, in their biomechanical study, on the importance of the distal membranous portion of the IOM, which constrained volar and dorsal instability of the radius at the DRUJ in all forearm rotation positions. Kihara and colleagues[22] indicated that the distal membranous portion of the IOM acted as a secondary stabilizer of the DRUJ when the dorsal and palmar radioulnar ligaments of the TFCC were cut. Although we cannot know whether these researchers were aware of the structure of the DOB, we postulate from their studies that the anatomical relationship of the DOB to the TFCC suggests that the DOB functions to stabilize the DRUJ in cooperation with the TFCC because the DOB forms a ligament within the distal membranous portion. However, further biomechanical investigation is needed to confirm our hypothesis.

The proximal oblique cord is a relatively well-investigated component,[13–15,23] whereas descriptions of this ligament are variable. Some authors[23] have insisted that the structure is a remnant or accessory head of the flexor pollicis longus muscle (Gantzer's muscle), whereas another author[13] has stated that this cord represents a thickening of the fascia overlying the supinator muscle or perhaps even a degenerate part of the supinator muscle. We have also observed that the proximal oblique cord shows morphological variations to some extent, ranging from thick to relatively membranous. Conflicting descriptions of function have been reported.[13–15] Martin[13] and Tubbs and colleagues[14] described the cord as being most taut in supination and lax in both the neutral position and pronation in human cadavers, suggesting action as a restraint on excessive supination motions. Conversely, Patel[15] reported that the proximal oblique cord became most taut in pronation rather than in supination in the forelimbs of quadrupedal primates, suggesting a possible role in maintaining elbow stability when such primates stand on their pronated forelimbs. All of these authors concluded that the proximal oblique cord has little function in humans.

The present study clarified precise attachment locations of all representative IOM ligaments. This information will be useful in planning proper graft placement in ligament reconstruction surgery and in future biomechanical research into the function of the IOM ligaments.

## REFERENCES

1. Hotchkiss RN, An K-N, Sowa DT, Basta S, Weiland AJ. An anatomic and mechanical study of the interosseous membrane of the forearm: pathomechanics of proximal migration of the radius. J Hand Surg 1989;14A:256–261.
2. Skahen JR III, Palmer AK, Werner FW, Fortino MD. The interosseous membrane of the forearm: anatomy and function. J Hand Surg 1997;22A:981–985.
3. Poitevin LA. Anatomy and biomechanics of the interosseous membrane: its importance in the longitudinal stability of the forearm. Hand Clin 2001;17:97–110.
4. Mori K. Experimental study on rotation of the forearm: functional anatomy of the interosseous membrane. J Jpn Orthop Assoc 1985; 59:611–622.
5. Nakamura T, Yabe Y, Horiuchi Y. Functional anatomy of the interosseous membrane of the forearm: dynamic changes during rotation. Hand Surg 1999;4:67–73.
6. Fujita M. An anatomical study on the interosseous membrane of the forearm. J Jpn Orthop Assoc 1995;69:938–950.
7. Schneiderman G, Meldrum RD, Bloebaum RD, Tarr R, Sarmiento A. The interosseous membrane of the forearm: structure and its role in Galeazzi fractures. J Trauma 1993;35:879–885.

8. Skahen JR III, Palmer AK, Werner FW, Fortino MD. Reconstruction of the interosseous membrane of the forearm in cadavers. J Hand Surg 1997A;22:986–994.
9. Rabinowitz RS, Light TR, Havey RM, Gourineni P, Patwardhan AG, Sartori MJ, et al. The role of the interosseous membrane and triangular fibrocartilage complex in forearm stability. J Hand Surg 1994A;19:385–393.
10. Birkbeck DP, Failla JM, Hoshaw J, Fyhrie DP, Schaffler M. The interosseous membrane affects load distribution in the forearm. J Hand Surg 1997;22A:975–980.
11. Pfaeffle HJ, Stabile KJ, Li ZM, Tomaino MM. Reconstruction of the interosseous ligament restores normal forearm compressive load transfer in cadavers. J Hand Surg 2005;30A:319–325.
12. Kapandji A. Biomechanics of pronation and supination of the forearm. Hand Clin 2001;17:111–122.
13. Martin BF. The oblique cord of the forearm. J Anat 1958;92:609–615.
14. Tubbs RS, O'Neil JT Jr, Key CD, Zarzour JG, Fulghum SB, Kim EJ, et al. Clin Anat 2007;20:411–415.
15. Patel BA. Form and function of the oblique cord *(chorda oblique)* in anthropoid primates. Primates 2005;46:47–57.
16. Chandler JW, Stabile KJ, Pfaeffle HJ, Li ZM, Woo SL-Y, Tomaino MM. Anatomic parameters for planning of interosseous ligament reconstruction using computer-assisted techniques. J Hand Surg 2003;28A:111–116.
17. Hollister AM, Gellman H, Waters RL. The relationship of the interosseous membrane to the axis of rotation of the forearm. Clin Orthop Relat Res 1994;298:272–276.
18. Nakamura T, Yabe Y, Horiuchi Y. In vivo MR studies of dynamic changes in the interosseous membrane of the forearm during rotation. J Hand Surg 1999;24B:245–248.
19. Nakamura T, Yabe Y, Horiuchi Y, Yamazaki N. Three-dimensional magnetic imaging of the interosseous membrane of forearm: a new method using fuzzy reasoning. Magn Reson Imaging 1999;17:463–470.
20. Nakamura T, Yabe Y, Horiuchi Y, Seki T, Yamazaki N. Normal kinematics of the interosseous membrane during forearm pronation-supination: a three-dimensional MRI study. Hand Surg 2000; 5:1–10.
21. Watanabe H, Berger RA, Berglund LJ, Zobitz ME, An KN. Contribution of the interosseous membrane to distal radioulnar joint constraint. J Hand Surg 2005;30A:1164–1171.
22. Kihara H, Short WH, Werner FW, Fortino MD, Palmer AK. The stabilizing mechanism of the distal radioulnar joint during pronation and supination. J Hand Surg 1995;20A:930–936.
23. Forster A. Uber den morphologischen Wert der Chorda oblique antebrachii anterior und der Chorda oblique antebrachii posterior. Z Morphol Anthropol 1905;8:62–79.

THE INTERNATIONAL JOURNAL OF MEDICAL ROBOTICS AND COMPUTER ASSISTED SURGERY
*Int J Med Robotics Comput Assist Surg* 2009; 5: 452–457.
Published online 1 September 2009 in Wiley InterScience (www.interscience.wiley.com). **DOI:** 10.1002/rcs.277

**ORIGINAL ARTICLE**

# Accuracy analysis of three-dimensional bone surface models of the forearm constructed from multidetector computed tomography data

Kunihiro Oka[1]*
Tsuyoshi Murase[1]
Hisao Moritomo[1]
Akira Goto[1]
Kazuomi Sugamoto[2]
Hideki Yoshikawa[1]

[1]*Department of Orthopaedic Surgery, Osaka University Graduate School of Medicine, Japan*

[2]*Department of Orthopaedic Biomaterial Science, Osaka University Graduate School of Medicine, Japan*

*Correspondence to: Kunihiro Oka, Department of Orthopaedic Surgery, Osaka University Graduate School of Medicine, 2-2 Yamada-oka, Suita, Osaka 565-0871, Japan. E-mail: oka-kunihiro@umin.ac.jp

*Accepted: 6 July 2009*

## Abstract

**Background** We developed an original computer program that simulates upper limb reconstruction surgery using three-dimensional (3D) bone models constructed from computed tomography (CT) data. However, the accuracy of a bone model has not been clarified, and radiation exposure from CT scanning posed a concern. The purpose of this study was to investigate the appropriate CT parameters required to reduce radiation exposure while maintaining the accuracy of 3D models of the forearm bones.

**Methods** Twelve dry forearm bones were used to investigate the accuracy of 3D bone models created from two different CT parameters. The accuracy was evaluated by measuring: (a) the discrepancy between the models constructed from low- and normal-dose CT parameters; (b) the error between actual surface data derived by a contact-type coordinate measuring machine and a 3D bone model; and (c) the difference between a 3D bone model constructed from a bare dry bone and a model constructed from the same bone embedded in a radio-opaque soft tissue substitute. CT dose index (CTDI) and dose-length product (DLP) were recorded to evaluate the radiation exposure.

**Results** The mean error between bone models constructed from two different CT parameters was 0.04 mm. CTDI and DLP for the normal-radiation dose condition were 9.3 and 563 mGy/cm and those for the low-radiation dose condition were 0.3 and 18 mGy/cm, respectively. The mean error between the bone models and scanning data from contact measurement was 0.45 mm. The mean error between a 3D model constructed from a dry bone and that constructed from the same bone embedded in a radio-opaque soft tissue substitute was 0.06 mm.

**Conclusions** 3D bone models constructed from low-radiation dose CT data demonstrated the same level of accuracy as those constructed from normal-radiation dose data. The present simulation system can produce 3D bone models with one-thirtieth of the normal radiation dose in the forearm.


**Keywords** radiation dose; computed tomography; upper extremity

## Introduction

The recent progress in computer technology and development of multidetector computed tomography (CT) has made it possible to use three-dimensional

(3D) preoperative simulations in total arthroplasty, spinal surgery and fracture operation (1–8). We have also developed a simulation system using 3D computer bone models constructed from CT data and demonstrated its clinical feasibility, particularly in upper extremity surgery (9–11). Precise computer bone models are a basic requirement for such systems and previous reports have discussed their accuracy in the lower extremity (12). The accuracy of a computer bone model of the upper extremity, however, has not been elucidated. Another concern about the long-term consequences of CT scanning is radiation exposure to the patient (13–17). Therefore, when using this system in a clinical application, it is essential to set radiation doses of CT at the lowest possible levels while maintaining the accuracy of a bone model. In preoperative simulations of the upper extremity, radiation exposure from CT scanning is expected to be considerably reduced below the normal dose used for diagnostic purposes, particularly because the volume of the extremity is small in comparison to the thorax, abdomen and pelvis. In addition, the contrast between the soft tissue and bone in the extremity is sufficiently distinct to discern the surface of the bone's cortex for constructing a computer bone model.

In the present study, we evaluated the accuracy of computer bone models constructed from CT data of the forearm using our system (9–11) and investigated whether CT scanning with a low radiation dose could effectively preserve the accuracy of a bone model.

# Materials and Methods

## Data acquisition

Twelve cadaveric dry forearm bones (six radii and six ulnae; Natural Human Bone, Sawbones®, Pacific Research Laboratories Inc., Vashon, WA, USA) were prepared for this study. CT scanning (LightSpeed Ultra16; General Electric, Waukesha, WI, USA) was performed on the bones with 0.625 mm thickness on contiguous slices, with pixels of 0.293 × 0.293 mm under two different conditions: tube voltage, tube current, pitch, and scan time were 120 kV, 50 mA, 0.562 : 1 and 1.0 s for the normal-radiation dose condition (18,19) and 120 kV, 10 mA, 1.750 : 1 and 0.5 s for the low-radiation dose condition, respectively. The values of weighted CT dose index (CTDI), which was the radiation dose for a single rotation of the CT scanner, and dose-length product (DLP), which was calculated by multiplying the CTDI for a scan sequence by the length of coverage along the specimen's length, corresponding to each acquisition protocol, were recorded during CT scanning. The Digital Imaging and Communications in Medicine (DICOM) data for 0.625 mm slices were sent to a workstation for analysis (Dell Precision™ Workstation 650, 266 MHz/2G; Dell Inc., Round Rock, TX, USA).

## Construction of bone surface model and accuracy analysis

The bone was segmented, and the 3D surface model was constructed with the threshold CT number set at 150 HU (20). 3D surface generation of the bone cortex was applied (21) using a VTK-based original computer program (Visualization Toolkit, Kitware Inc., Clifton Park, NY, USA). Then, by cancelling the bone marrow data, we completed a surface model of the bone (Figure 1A–C). Thus, 3D surface models of radii and ulnae were constructed in each dose condition (Figure 2A, B). Surface-based registration was performed by independently implementing the iterative closest point algorithm (22,23) with the least-squares method to match the two computer bone surface models constructed under different radiation dose conditions. The error between the two models was then calculated (Figure 2C). The formula to compute errors between the two models is as follows: the point set $P$ with $N_p$ points $\{\overrightarrow{p_i}\}$ from the data shape and model shape $X$ (with $N_X$ supporting geometric primitives: points, lines or triangles) are given. Compute the closest points: $Y_k = C(P_k, X)$, [cost: $0(N_p\ N_X)$ worst case, $0(N_p \log N_X)$ average]. The mean squared error $e_k$ of that correspondence is given by:

$$e_k = \frac{1}{N_p} \sum_{i=1}^{N_p} \|\overrightarrow{y_{1k}} - \overrightarrow{p_{1k}}\|^2$$

## Error between bone surface model and actual bone

Next, the difference between an actual dry bone and its 3D surface model was evaluated. First, the 3D shapes of the bones were measured using a contact-type coordinate-measuring machine (Cyclone, Renishaw, New Mills, UK) (Figure 3A, B), which had an accuracy of <50 μm. The bone measurements were then saved as 2000 points of data (Figure 4A). We defined the 3D points data of the bone surface measured by the contact-type coordinate-measuring machine as the gold standard of accuracy. Surface-based registration was used to match these data points with those of the bone surface model constructed from the CT data under the low-radiation dose condition, and the error between them was calculated (Figure 4B).

## Evaluation of soft tissue influence

The final evaluation of the accuracy of the computer bone model was performed by comparing the 3D surface model constructed from the CT data of a dry bone and that constructed from the CT data of a forearm phantom, which was prepared by embedding the same dry bone in a radiation-absorbable soft tissue substitute. This validation procedure was conducted to determine how soft tissue influences the accuracy of the computer bone model. The phantom was prepared by embedding dry bones

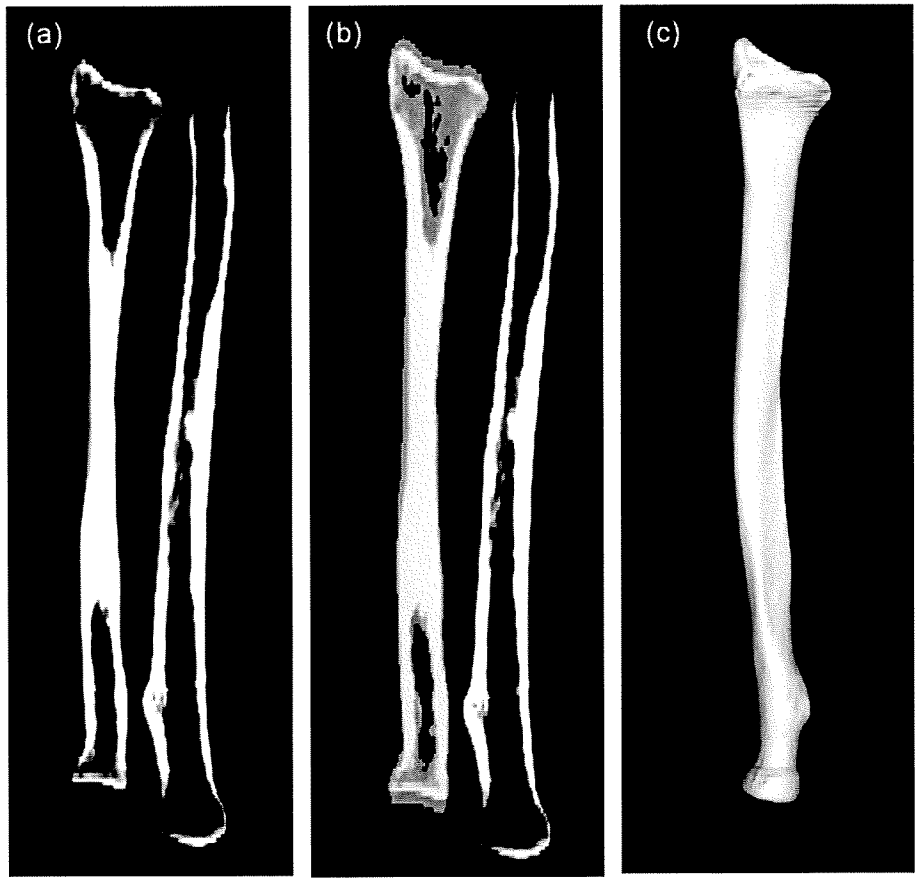


**Figure 1. With an image obtained from CT reconstruction (a), the malunited bone was segmented (b) and a 3D surface model was constructed using an original computer program (c)**

in a soft tissue substitute made of polyurethane resin and phosphoric acid $[(C_2H_4ClO)_3PO]$, which had a CT number of 0 HU (SZ-50; Kyoto Kagaku Co. Ltd., Kyoto, Japan) (24), after scanning the bones with CT. The bones were then re-inspected by CT in the low-radiation dose condition, and the 3D bone model was constructed with a threshold value of 150 HU. Surface-based registration was performed using the computer program with the bone surface models created from the CT data of the forearm phantom and the dry bone to calculate the error between them.

## Results

The mean error between the 3D bone surface models constructed under two different CT conditions (i.e. normal- and low-radiation doses) was $0.04 \pm 0.01$ mm (Table 1). These results indicate that low- and normal-radiation-dose CT parameters provide an almost identical 3D bone surface model. CTDI and DLP with the normal-radiation dose resulted in 9.3 and 563 mGy/cm, respectively. With the low-radiation dose, CTDI and DLP were 0.3 and 18 mGy/cm. The radiation dose of the low-dose condition was about one-thirtieth of the normal-dose condition. The mean error between the 3D bone models constructed from the CT data and scanning data of actual measurements of a bone surface using a contact-type measuring machine was $0.46 \pm 0.03$ mm (Table 1). The mean error between a 3D surface model constructed from a dry bone and that constructed from a phantom embedded in a radiation-absorbable soft tissue substitute was $0.06 \pm 0.01$ mm (Table 1).

The 3D bone surface model constructed from low-radiation dose CT data had an accuracy of $<0.5$ mm, and the influence of soft tissue on the construction of this model was negligible.

## Discussion

Although radiation exposure to the human body poses a significant problem (16,17), the benefits of CT as a clinical diagnostic tool and in preoperative surgical planning may outweigh its adverse effects in many situations. With the implementation of 3D bone models constructed from CT data in recent orthopaedic surgeries, the demand for CT has been increasing. They have been used in a simulation–navigation system for implant arthroplasties of the hip and knee joints (25–30). In spinal surgery, CT is used to navigate the placement of pedicle screws (31–34). We also developed a 3D computer simulation system for corrective osteotomy for malunited fractures and reported

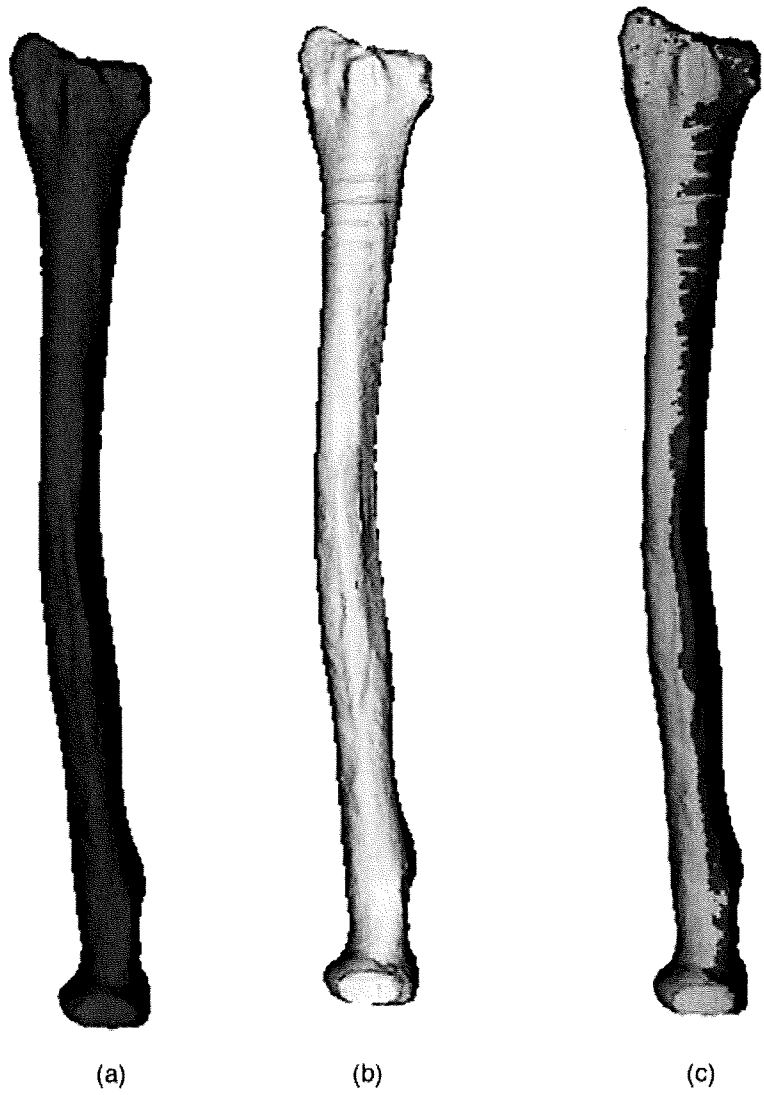


**Figure 2. 3D bone surface models constructed from CT data in (a) normal-radiation and (b) low-radiation doses. (a) and (b) were matched to evaluate the error between them (c)**

encouraging clinical results in upper extremity cases (10,11).

However, there are two issues to be solved concerning the use of 3D bone models constructed from CT data. The first is the accuracy of a bone model itself. Although accuracy in lower extremity has been reported (12), it has never been clarified in the upper extremity. Therefore, we had first planned to make an error analysis between a 3D bone model and actual measurement of the forearm bone. The other concern is the radiation exposure during CT scanning. When considering the accuracy of a computer bone model, it is also desirable to use as little radiation as possible in order to avoid its adverse effects to the human body. Appropriate CT parameters required for construction of bone models should be specified not only to create a bone model with high accuracy, but also to reduce radiation exposure. Bonel *et al.* (18) investigated the optimal CT parameters to achieve diagnostic image quality with minimum radiation exposure for the wrist and reported that a low tube voltage of 80 kV, a tube current of 100 mA, a thickness of 1.0 mm, a pitch of 1.5 and a rotation time of 0.75 s were adequate. However, if CT is taken for the purpose of creating a 3D bone surface model and not for diagnostic purposes, even less radiation exposure may be adequate because the contrast between the bone and soft tissue is sufficiently distinct. Consequently, we investigated the accuracy of a 3D bone surface model created from CT with a lower radiation dose; CT parameters were set at one-tenth of the tube current, seven-sixths of the pitch and two-thirds of the scan time of clinically established parameters (18). As a result, the radiation exposure from CT scanning with this system was estimated to be as low as one-thirtieth of the standard scanning dose. The 3D bone surface models using low-radiation dose CT parameters were as precise as those using normal-radiation dose CT parameters within 0.5 mm when compared to the actual measurement data, and were thought accurate enough to be used in preoperative simulation and navigation surgeries (20,35–38). The results of the current study also demonstrated that the influence of soft tissue on 3D bone surface models was negligible. The CT number

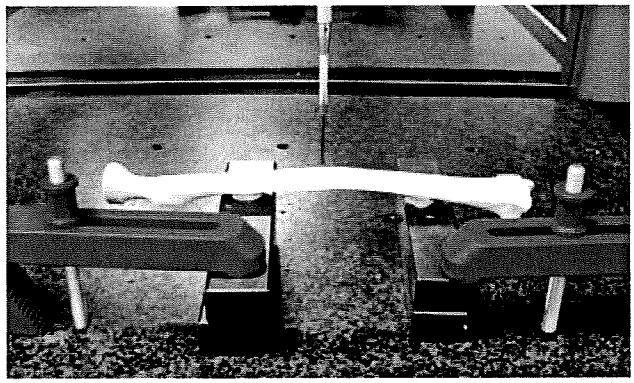

(a)

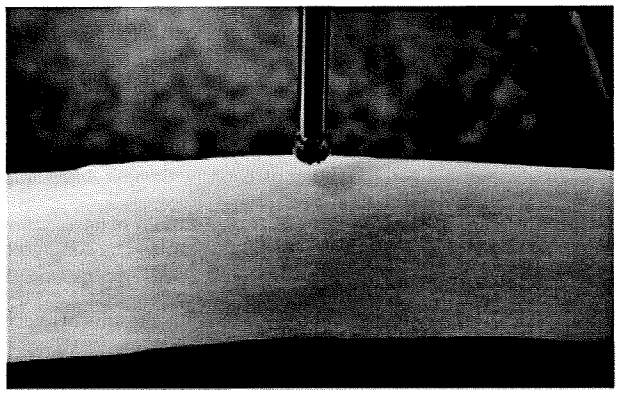

(b)

Figure 3. The contact-type coordinate-measuring machine used to scan the surface of the radius with a probe to create digital 3D models represented by a number of data points (a, b)

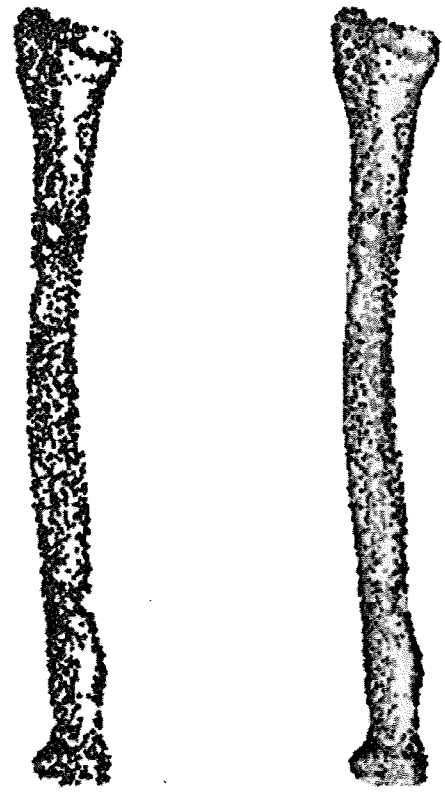

(a) (b)

Figure 4. Data points of bone surface of a radius measured by a coordinate measuring machine (a). The data points and the 3D bone surface model constructed with low-radiation dose were matched (b)

of bone cortex is significantly higher (1000 HU) when compared to soft tissues such as muscle (30–60 HU), blood (50 HU) and fat (−100 HU). This increased CT number allows the contour line of the bone cortex to be clearly recognized without noise when binarization is performed at a threshold value of 150 HU. In addition, the forearm requires less radiation to acquire adequate image quality, since it has a smaller volume compared to that of the thorax, pelvis, femur and tibia.

In this study, the interference posed by the spine and pelvis, which could influence the image quality of the forearm during the actual scanning, was not taken into account. However, their influence was considered negligible so long as the patient was in a prone position and the forearm was elevated over the head during scanning.

Considering these results, we conclude that low-radiation CT scan parameters will be well tolerated, and the bone surface model obtained from it is sufficiently accurate for clinical use.

Table 1. Error of 3D bone models in each condition (mm)

| No. | Bone | Error between bone models constructed from: 3D computer model and point data | Normal and low-dose CT scanning | CT data of dry bone and phantom* |
|---|---|---|---|---|
| 1 | | 0.41 | 0.05 | 0.05 |
| 2 | | 0.42 | 0.05 | 0.05 |
| 3 | Radius | 0.43 | 0.04 | 0.05 |
| 4 | | 0.43 | 0.03 | 0.06 |
| 5 | | 0.44 | 0.05 | 0.06 |
| 6 | | 0.49 | 0.04 | 0.06 |
| 7 | | 0.47 | 0.06 | 0.07 |
| 8 | | 0.47 | 0.04 | 0.08 |
| 9 | Ulna | 0.49 | 0.05 | 0.07 |
| 10 | | 0.46 | 0.04 | 0.07 |
| 11 | | 0.46 | 0.04 | 0.05 |
| 12 | | 0.49 | 0.04 | 0.07 |
| Average | | 0.46 ± 0.03 | 0.04 ± 0.01 | 0.06 ± 0.01 |

*A phantom was prepared by embedding the same dry bone in a radiation absorbable soft tissue substitute.

## Acknowledgement

The authors acknowledge the assistance of computer programmer Ryoji Nakao of the Department of Orthopaedic Surgery, Osaka University Graduate School of Medicine, during parts of the experimental procedure.

## References

1. Athwal GS, Ellis RE, Small CF, *et al.* Computer-assisted distal radius osteotomy. *J Hand Surg [Am]* 2003; **28**(6): 951–958.

2. Beckmann J, Goetz J, Baethis H, *et al.* Precision of computer-assisted core decompression drilling of the femoral head. *Arch Orthop Trauma Surg* 2006; **126**(6): 374–379.
3. Chen E, Goertz W, Lill CA. Implant position calculation for acetabular cup placement considering pelvic lateral tilt and inclination. *Comput Aided Surg* 2006; **11**(6): 309–316.
4. Ellis RE, Tso CY, Rudan JF, *et al.* A surgical planning and guidance system for high tibial osteotomy. *Comput Aided Surg* 1999; **4**(5): 264–274.
5. Kanlic EM, Delarosa F, Pirela-Cruz M. Computer assisted orthopaedic surgery – CAOS. *Bosn J Basic Med Sci* 2006; **6**(1): 7–13.
6. Shimizu T, Fujioka F, Gomyo H, *et al.* Three-dimensional starch model for simulation of corrective osteotomy for a complex bone deformity: a case report. *Foot Ankle Int* 2003; **24**(4): 364–367.
7. Wong KC, Kumta SM, Chiu KH, *et al.* Precision tumour resection and reconstruction using image-guided computer navigation. *J Bone Joint Surg Br* 2007; **89**(7): 943–947.
8. Yamazaki M, Akazawa T, Okawa A, *et al.* Usefulness of three-dimensional full-scale modeling of surgery for a giant cell tumor of the cervical spine. *Spinal Cord* 2007; **45**(3): 250–253.
9. Murase T, Moritomo H, Goto A, *et al.* Does three-dimensional computer simulation improve results of scaphoid nonunion surgery? *Clin Orthop Relat Res* 2005; **434**: 143–150.
10. Murase T, Oka K, Moritomo H, *et al.* Three-dimensional corrective osteotomy of malunited fractures of the upper extremity with use of a computer simulation system. *J Bone Joint Surg Am* 2008; **90**: 2375–2389.
11. Oka K, Moritomo H, Goto A, *et al.* Corrective osteotomy for malunited intra-articular fracture of the distal radius using a custom-made surgical guide based on three-dimensional computer simulation: case report. *J Hand Surg [Am]* 2008; **33**(6): 835–840.
12. Gelaude F, Vander Sloten J, Lauwers B. Accuracy assessment of CT-based outer surface femur meshes. *Comput Aided Surg* 2008; **13**(4): 188–199.
13. Hall EJ, Brenner DJ. Cancer risks from diagnostic radiology. *Br J Radiol* 2008; **81**(965): 362–378.
14. Paul JF, Abada HT. Strategies for reduction of radiation dose in cardiac multislice CT. *Eur Radiol* 2007; **17**(8): 2028–2037.
15. Kalra MK, Maher MM, Saini S. Multislice CT: update on radiation and screening. *Eur Radiol* 2003; **13**: (suppl 5): M129–133.
16. Berrington de Gonzalez A, Darby S. Risk of cancer from diagnostic X-rays: estimates for the UK and 14 other countries. *Lancet* 2004; **363**(9406): 345–351.
17. Kalra MK, Maher MM, Toth TL, *et al.* Strategies for CT radiation dose optimization. *Radiology* 2004; **230**(3): 619–628.
18. Bonel HM, Jager L, Frei KA, *et al.* Optimization of MDCT of the wrist to achieve diagnostic image quality with minimum radiation exposure. *AJR Am J Roentgenol* 2005; **185**(3): 647–654.
19. Bush CH, Gillespy T III, Dell PC. High-resolution CT of the wrist: initial experience with scaphoid disorders and surgical fusions. *AJR Am J Roentgenol* 1987; **149**(4): 757–760.
20. Sugano N, Sasama T, Sato Y, *et al.* Accuracy evaluation of surface-based registration methods in a computer navigation system for hip surgery performed through a posterolateral approach. *Comput Aided Surg* 2001; **6**(4): 195–203.
21. Lorensen WE, Cline HE. Marching cubes: a high resolution 3D surface construction algorithm. *Comput Graph* 1987; **21**: 163–169.
22. Besl PJ, Mackay N. A method for registration of 3D shapes. *IEEE Trans Patt Anal* 1992; **14**: 239–256.
23. Audette MA, Ferrie FP, Peters TM. An algorithmic overview of surface registration techniques for medical imaging. *Med Image Anal* 2000; **4**(3): 201–217.
24. Shirotani T. Realistic torso phantom for calibration of *in vivo* transuranic nuclide-counting facilities. *J Nucl Sci Technol* 1988; **25**(11): 875–883.
25. Decking R, Markmann Y, Fuchs J, *et al.* Leg axis after computer-navigated total knee arthroplasty: a prospective randomized trial comparing computer-navigated and manual implantation. *J Arthroplasty* 2005; **20**(3): 282–288.
26. Delp SL, Stulberg SD, Davies B, *et al.* Computer assisted knee replacement. *Clin Orthop Relat Res* 1998; **354**: 49–56.
27. DiGioia AM, Jaramaz B, Blackwell M, *et al.* The Otto Aufranc Award. Image guided navigation system to measure intraoperatively acetabular implant alignment. *Clin Orthop Relat Res* 1998; **355**: 8–22.
28. La Palombara PF, Fadda M, Martelli S, *et al.* Minimally invasive 3D data registration in computer and robot assisted total knee arthroplasty. *Med Biol Eng Comput* 1997; **35**(6): 600–610.
29. Langlotz F, Stucki M, Bachler R, *et al.* The first twelve cases of computer assisted periacetabular osteotomy. *Comput Aided Surg* 1997; **2**(6): 317–326.
30. Ybinger T, Kumpan W, Hoffart HE, *et al.* Accuracy of navigation-assisted acetabular component positioning studied by computed tomography measurements: methods and results. *J Arthroplasty* 2007; **22**(6): 812–817.
31. Amiot LP, Lang K, Putzier M, *et al.* Comparative results between conventional and computer-assisted pedicle screw installation in the thoracic, lumbar, and sacral spine. *Spine* 2000; **25**(5): 606–614.
32. Girardi FP, Cammisa FP Jr, Sandhu HS, *et al.* The placement of lumbar pedicle screws using computerised stereotactic guidance. *J Bone Joint Surg Br* 1999; **81**(5): 825–829.
33. Laine T, Lund T, Ylikoski M, *et al.* Accuracy of pedicle screw insertion with and without computer assistance: a randomised controlled clinical study in 100 consecutive patients. *Eur Spine J* 2000; **9**(3): 235–240.
34. Merloz P, Tonetti J, Pittet L, *et al.* Computer-assisted spine surgery. *Comput Aided Surg* 1998; **3**(6): 297–305.
35. Biant LC, Yeoh K, Walker PM, *et al.* The accuracy of bone resections made during computer navigated total knee replacement. Do we resect what the computer plans we resect? *Knee* 2008; **15**(3): 238–241.
36. Koestler W, Sidler R, Gonzalez Ballester MA, *et al.* A feasibility study of computer-assisted bone graft implantation for tissue-engineered replacement of the human ankle joint. *Comput Aided Surg* 2008; **13**(4): 207–217.
37. Ruppin J, Popovic A, Strauss M, *et al.* Evaluation of the accuracy of three different computer-aided surgery systems in dental implantology: optical tracking vs. stereolithographic splint systems. *Clin Oral Implants Res* 2008; **19**(7): 709–716.
38. Tamura Y, Sugano N, Sasama T, *et al.* Surface-based registration accuracy of CT-based image-guided spine surgery. *Eur Spine J* 2005; **14**(3): 291–297.

Interface focus

*J. R. Soc. Interface* (2009) **6**, S341–S348
doi:10.1098/rsif.2008.0425.focus
*Published online* 23 December 2008

REVIEW

# Interconnected porous hydroxyapatite ceramics for bone tissue engineering

**Hideki Yoshikawa*, Noriyuki Tamai, Tsuyoshi Murase and Akira Myoui**

*Department of Orthopaedic Surgery, Osaka University Graduate School of Medicine, 2-2 Yamadaoka, Suita 565-0871, Japan*

Several porous calcium hydroxyapatite (HA) ceramics have been used clinically as bone substitutes, but most of them possessed few interpore connections, resulting in pathological fracture probably due to poor bone formation within the substitute. We recently developed a fully interconnected porous HA ceramic (IP-CHA) by adopting the 'foam-gel' technique. The IP-CHA had a three-dimensional structure with spherical pores of uniform size (average 150 μm, porosity 75%), which were interconnected by window-like holes (average diameter 40 μm), and also demonstrated adequate compression strength (10–12 MPa). In animal experiments, the IP-CHA showed superior osteoconduction, with the majority of pores filled with newly formed bone. The interconnected porous structure facilitates bone tissue engineering by allowing the introduction of mesenchymal cells, osteotropic agents such as bone morphogenetic protein or vasculature into the pores. Clinically, we have applied the IP-CHA to treat various bony defects in orthopaedic surgery, and radiographic examinations demonstrated that grafted IP-CHA gained radiopacity more quickly than the synthetic HA in clinical use previously. We review the accumulated data on bone tissue engineering using the novel scaffold and on clinical application in the orthopaedic field.

**Keywords: bone; ceramics; hydroxyapatite; tissue engineering; mesenchymal cell**

## 1. INTRODUCTION

When bone grafts are required for bony defects in orthopaedic surgery, autogenous bone grafting has been the gold standard because of its obvious advantages in osteogenic potential, mechanical properties and the lack of adverse immunological response. On the other hand, autogenous bone grafting has some limitations, such as the requirement of additional surgery for harvesting, the availability of sufficient grafts in size and shape and the risk of donor-site morbidity (Banwart *et al.* 1995; Arrington *et al.* 1996), which may include long-lasting pain, fracture, nerve damage and infection. Although allogeneic bone is widely used in the USA, its use is quite limited in Japan, accounting for as little as 3 per cent of procedures (Prolo & Rodrigo 1985), presumably owing to religious difficulties with using tissue from other people or corpses, as well as the lack of a well-organized tissue bank system. In addition, allograft carries the risk of transmission of occult disease, or a host immune response, which can sometimes result in complete resorption of the grafts. Therefore, many kinds of biomaterials have been developed as bone substitutes, such as hydroxyapatite (HA), alumina, zirconia, bioglass, polymers, metal, and organic or inorganic bone substitutes (Sartoris *et al.* 1986; Bucholz *et al.* 1987; Fujibayashi *et al.* 2003; Nishikawa & Ohgushi 2004).

HA ceramics have been used extensively as a substitute in bone grafts (Holmes *et al.* 1987; Bucholz *et al.* 1989), because the crystalline phase of natural bone is similar to HA. Since the 1980s, blocks and granules of porous calcium HA ceramics (CHA) have been used in orthopaedic, dental or craniofacial surgery (Uchida *et al.* 1990; Yoshikawa & Uchida 1999; Matsumine *et al.* 2004). However, there are few reports which indicate that the pores of implanted CHA are totally filled with newly formed host bone (Nakasa *et al.* 2005), probably owing to the closed structures of these CHA with few interpore connections (Ayers *et al.* 1998).

Therefore, the development of porous CHA with interpore connections of adequate diameter as well as adequate strength has long been expected as an ideal bone substitute (Roy *et al.* 2003; Simon *et al.* 2003, 2007, 2008). We recently developed a fully interconnected porous HA ceramic (IP-CHA; porosity 75%, average pore size 150 μm and average interconnections 40 μm) by adopting a 'foam-gel' technique, crosslinking polymerization that gelatinizes through the foam-like slurry in a moment (Tamai *et al.* 2002). The interconnected porous structure facilitates bone

*Author for correspondence (yhideki@ort.med.osaka-u.ac.jp).

One contribution of 10 to a Theme Supplement 'Japanese biomaterials'.

*Received* 11 November 2008
*Accepted* 28 November 2008

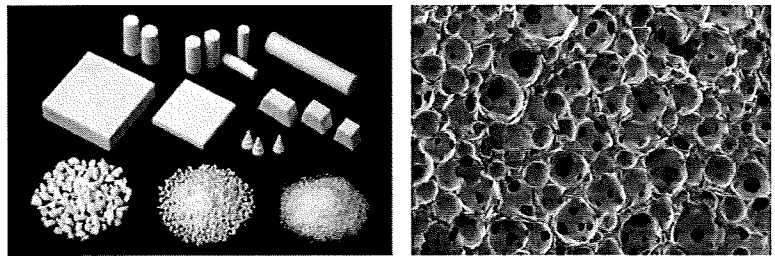

Figure 1. Interconnected porous HA ceramics (IP-CHA). (*a*) Macroscopic images of IP-CHA. The materials were manufactured by Covalent Materials Corporation. (*b*) SEM image of the microstructures of IP-CHA. Spherical pores (100–200 μm in diameter) are divided by thin walls and interconnected by interpores (10–80 μm in diameter).

tissue engineering by allowing the introduction of mesenchymal cells, osteotropic agents or vasculature into the pores. In this review, we report a new bone tissue engineering system using IP-CHA, a preliminary clinical result in patients treated with IP-CHA and a new clinical trial using a prefabricated IP-CHA in orthopaedic surgery.

## 2. CONVENTIONAL HYDROXYAPATITE CERAMICS IN JAPAN

The crystalline phase of natural bone is basically HA, and HA ceramics have been used extensively as a substitute in bone grafts. The ceramics are available as dense or porous types and the shape types are granular or block-like. Different pore sizes, porosities and strengths are available. Here, we describe four types of conventional HA (the first generation) that were used clinically.

— *BONEFIL* (*Mitsubishi Materials Corporation*). The types of ceramics are porous blocks and porous granules, and are most often used in orthopaedics. The sintering temperature is 900°C and the compression strength is 15 MPa/2 to 3 MPa. The pore shape is spongiose and the pore size is 200–300 μm. The degree of porosity is 60–70 per cent.

— *BONETITE* (*Mitsubishi Materials Corporation*). The types of ceramics are porous blocks and dense granules, and are most often used in dental surgery. The sintering temperature is 1200°C. The pore shape is spongiose and the pore size is 200 μm. The degree of porosity is 70 per cent.

— *BONECERAM* (*Sumitomo Osaka Cement Co. Ltd*). Porous block and porous granular types of the ceramics are available as BONECERAM-P. The sintering temperature is 1150°C. The compression strength is 44.1–68.6 MPa and the bending strength is 12.7–19.6 MPa. The pore shape is spherical and the pore size is 50–300 μm. The degree of porosity is 35–48 per cent. Dense block types of the ceramics having a high mechanical strength are available as BONECERAM-K. The sintering temperature is 1150°C. The bending strength is over 58.8 MPa.

— *APACERAM* (*PENTAX Corporation*). The types of ceramics are both dense and porous. The porous ceramic has a degree of porosity of 15–60 per cent. The sintering temperature is 1200°C. The compression and bending strengths vary from 16 to 250 MPa and 8 to 47 MPa, respectively. The better mechanical properties are associated with a decrease in the degree of porosity. The pore shape is spherical. The pore structure is an interconnected bimodal pore configuration consisting of a combination of 300 μm macropores and 2 μm micropores. The dense HA has a degree of porosity of less than 0.8 per cent. The sintering temperature is 1050°C. The compression and bending strengths are 750 and 210 MPa, respectively. Clinical applications began in 1985, with approximately 5000 clinical uses of APACERAM ceramics (custom-designed porous type plate) in cranioplasty since then. The numbers of clinical cases involving spinal surgery and ENT surgery with ear ossicle substitutes are 70 000 and 20 000, respectively.

All four of these manufactured HA ceramics are without effective interpore connections and essentially non-resorbable.

## 3. INTERCONNECTED POROUS HYDROXYAPATITE CERAMICS

The conventional method used to manufacture synthetic porous HA ceramics is by sintering a HA slurry mixed with organic polymer beads (Uchida *et al.* 1984). The polymer beads melt and vaporize during the sintering process, eventually leaving pores in the ceramic material. However, the pores resulting from this method are irregular in size and shape and not fully interconnected with one another. Together with Covalent Materials Corporation, MMT Co. Ltd and National Institute for Materials Science, Biomaterials Center, we developed an IP-CHA (porosity 75%, average pore size 150 μm and average interpore connections 40 μm) by adopting the foam-gel technique (figure 1; Tamai *et al.* 2002). This approach involves a crosslinking polymerization step that gelatinizes the foam-like CHA slurry in a rapid manner, thus promoting the formation of an interconnected porous structure. Briefly, the new method is as follows. (i) Slurry preparation: the slurry was prepared by mixing HA (60 wt%) with a crosslinking substrate (polyethyleneimine, 40 wt%). (ii) Foaming and gelatinization: the slurry was mixed with a foaming agent (polyoxyethylene lauryl ether, 1 wt%) and stirred until the mixture had a foamy appearance. Pore size was controlled by regulating the stirring time.

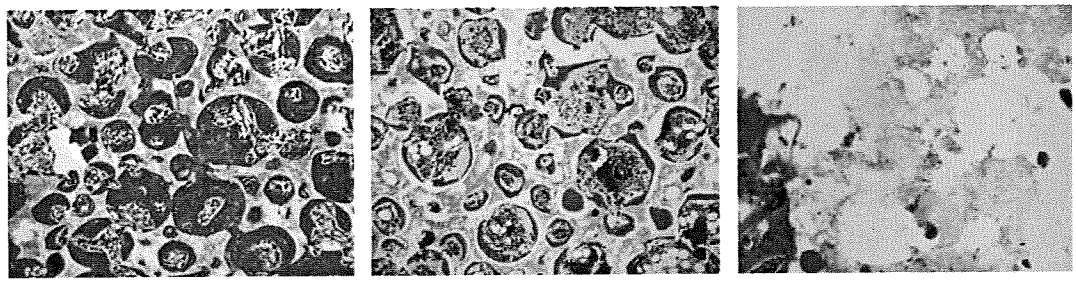

Figure 2. New bone formation within the IP-CHA in rabbit femoral condyle (HE staining×100). (*a*) Most of the pores were filled with newly formed bone at 2 weeks and (*b*) bone marrow formation was detected at 6 weeks. (*c*) In contrast, bone formation was not observed in the control group (conventional HA without interpore connections).

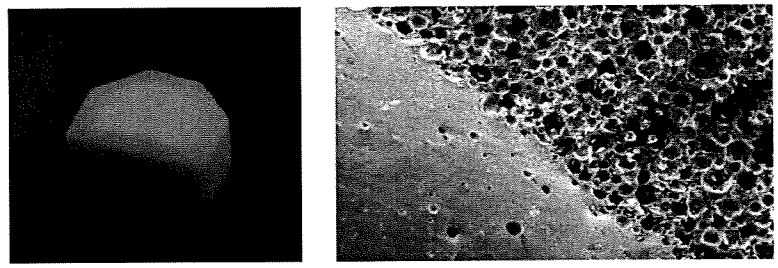

Figure 3. (*a*) Macroscopic and (*b*) microscopic (SEM) images of the solid/interconnected porous HA composite. Mechanical strength of the solid and the porous part is 550–570 and 10–12 MPa, respectively.

(iii) Gelatinization: to gelatinize the foamed slurry, another water-soluble crosslinking agent (polyfunctional epoxy compound) was added and the mixture was cast by pouring into a mould. The porous structure stabilized in less than 30 min. The foamy HA gel was removed from the mould, dried and sintered at 1200°C.

Scanning electron microscopy (SEM) analysis revealed that most of the IP-CHA pores were spherical, similar in size, approximately 100–200 μm in diameter, and showed uniform connections with one another. The wall surface of IP-CHA was very smooth and HA particles were aligned closely to one another and bound tightly.

The majority of the interpore connections ranged from 10 to 80 μm in diameter, with a maximum peak of approximately 40 μm, which would theoretically allow cell migration or tissue invasion from pore to pore (Steinkamp *et al.* 1976). Interpore connections larger than 10 μm accounted for as much as 91 per cent of the total porosity in IP-CHA. The calculated available porosity, the proportional volume of pores in the material that were connected by interpore connections larger than 10 μm in diameter, was 73.4 per cent (total porosity)×0.91=67.1 per cent. The compression strength was 12 MPa, while the compression strength of cancellous bone is 1–12 MPa (Martin *et al.* 1993).

## 4. OSTEOCONDUCTION *IN VIVO*

Macroporosity is known to influence the biological performance of calcium phosphate *in vivo*. Holmes *et al.* (1988) reported that pores of approximately 100 μm in diameter could provide a framework for bone growth into the pore, which then becomes vascularized easily. Most of the pores of IP-CHA are large enough to show such criteria and, more importantly, the pores are fully interconnected and more likely to allow bone ingrowth. Cylindrical blocks (6 mm in diameter) of IP-CHA were implanted into rabbit femoral condyle, and the bone ingrowth was histologically analysed (Tamai *et al.* 2002; Myoui *et al.* 2004; Yoshikawa & Myoui 2005). Within six weeks after implantation of IP-CHA, mature bone ingrowth was seen in most of the pores throughout the block. In the pores, bone, bone marrow formation through interpore connections with osteoblastic rimming and vessels were all observed (figure 2). We also examined the sequential change in the compression strength of IP-CHA implanted in rabbit femoral condyle. The initial compression strength of IP-CHA was approximately 10–12 MPa. The implanted IP-CHA steadily increased its compression strength with time until nine weeks after implantation, finally reaching a value of approximately 30 MPa (Tamai *et al.* 2002).

Recently, in order to reinforce its initial mechanical strength, we have developed a novel composite with the solid form of HA. Figure 3 shows the macroscopic and microscopic images of the solid/interconnected porous HA composite (Kaito *et al.* 2006). The mechanical strength of the solid part is 550–570 MPa, thus the solid part may correspond to cortical bone, and the porous part to cancellous bone. We constructed an implant and used a canine lumbar interbody fusion model to evaluate bone conduction of the implant and its efficacy for bony fusion. Six months after the surgery, the implant exhibited almost the same efficacy for bony fusion as iliac bone grafts. Moreover, pores of the porous part of the implant were completely filled with newly formed bone and bone marrow cells (Kaito *et al.* 2006).

## 5. CLINICAL APPLICATION IN ORTHOPAEDIC SURGERY

HA is a useful material to fill bone defects in treating benign bone tumours because of its biocompatibility,

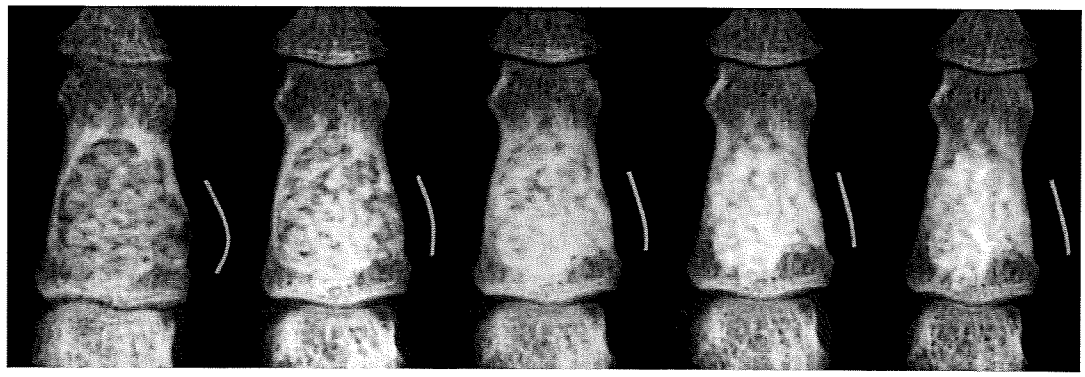

Figure 4. Clinical application of IP-CHA in the treatment of patients with bone tumours. An enchondroma of mid-phalanx, 28-year-old male. As radiodensity increased, the affected bone was remodelled, and the expansive deformity was self-corrected. (*a*) Just after surgery, (*b*) 3 months after surgery, (*c*) 6 months after surgery, (*d*) 12 months after surgery and (*e*) 27 months after surgery.

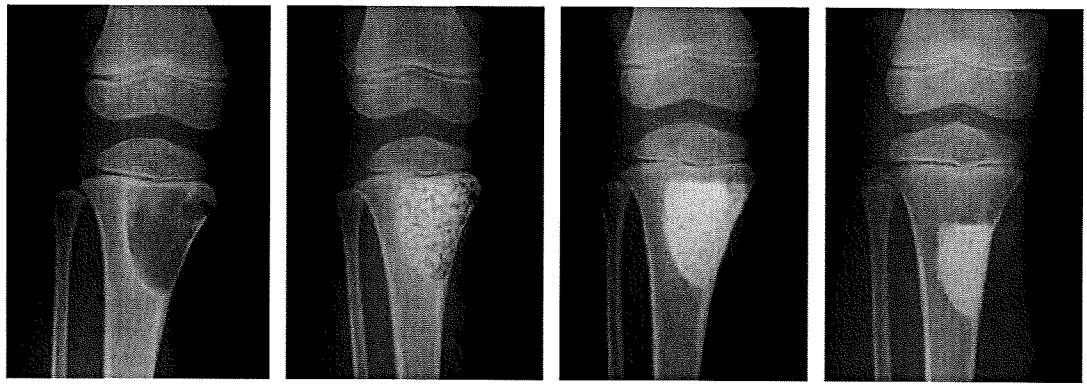

Figure 5. Clinical application of IP-CHA in the treatment of patients with bone tumours. A simple bone cyst of proximal tibia, 5-year-old boy. (*a*) Before surgery, (*b*) just after surgery, (*c*) 6 months after surgery and (*d*) 36 months after surgery.

osteoconduction and convenience, and it eliminates the need for additional surgery for harvesting autograft, as we reported previously (Uchida *et al.* 1990; Yoshikawa & Uchida 1999; Matsumine *et al.* 2004). However, as a late complication, pathological fractures of the implanted sites have been reported (Yoshikawa & Uchida 1999; Matsumine *et al.* 2004). This is probably due to poor bone ingrowth in the material as a result of poor incorporation of the material into the host bone. We applied IP-CHA as a bone substitute for the treatment of 59 patients with benign bone tumours at the Osaka University Hospital and its affiliated hospitals. The average age of patients was 32 years (range 5–75 years). The tumours were located in the upper extremities in 25 patients, lower extremities in 27 and pelvis in 7. The mean follow-up period was 46 months (range 32–60 months). After adequate removal of the tumours, IP-CHA blocks and/or granules of 2–5 mm in diameter were used to fill the bony defects. We also used IP-CHA to fill 12 cystic lesions with rheumatoid arthritis (Shi *et al.* 2006). None of the patients showed any signs of inflammatory reaction, rejection, infection or abnormal results in blood tests. Neither pathological fracture nor deformity was observed at the implanted site based on radiographic examinations during the follow-up period. The radiographic examinations were periodically carried out and revealed that the radiolucent line between the implanted IP-CHA and host bone tended to decrease with time after surgery and eventually disappeared (figure 4). The radiographic density at the implanted site increased with time and the IP-CHA granules appeared to fuse with one another, eventually forming a dense radiopaque shadow. Interestingly, longitudinal bone growth was not disturbed even when IP-CHA was implanted in close proximity to the growth plate of children (figure 5). Gadolinium-enhanced MRI showed a ring enhancement at the periphery of the implant (data not shown) and the area with enhancement advanced towards the centre of the implant, indicating that bone regeneration with blood supply might occur within the IP-CHA.

The IP-CHA can be prefabricated into specific sizes and shapes to match bone defects. We did this to make an implant, which was, in advance, planned and reconstructed with a computer-aided design/manufacturing (CAD/CAM) system. A three-dimensional image was reconstructed with the CT data of the estimated bony defect, and the IP-CHA was fabricated by a three-dimensional milling machine (Roland DG, MDX-20; figure 6). We have used the prefabricated IP-CHA for various bony defects in orthopaedic surgery, and obtained a satisfactory clinical outcome.

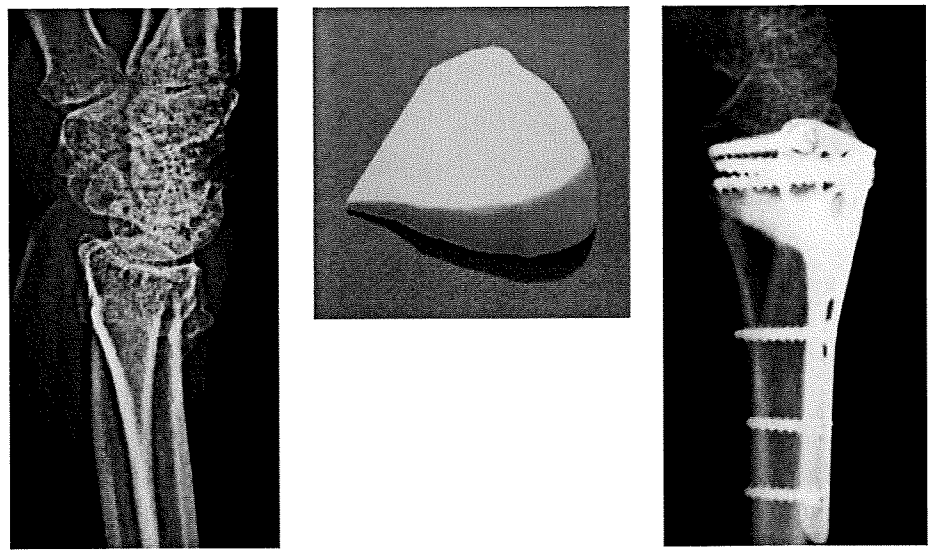

Figure 6. Correction osteotomy for malunited fracture of the distal radius, 48-year-old woman. (*a*) Preoperative X-ray image of the affected radius, six months after the fracture of the distal radius. (*b*) Prefabricated IP-CHA. A three-dimensional image was reconstructed with the CT data of the estimated bony defect after correction, and the IP-CHA was fabricated by a three-dimensional milling machine (Roland DG, MDX-20). (*c*) Post-operative X-ray image, a year after surgery. The malalignment was satisfactorily corrected by the surgery using the prefabricated IP-CHA and a metal plate.

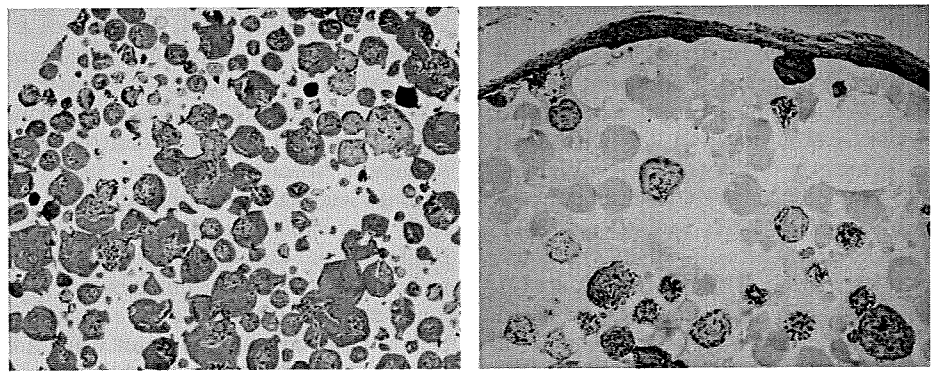

Figure 7. Bone tissue engineering by mesenchymal stem cells (HE staining×40). (*a*) At eight weeks after implantation, extensive bone volume was detected not only in the surface pore areas but also in the centre pore areas of IP-CHA. (*b*) In the control group (conventional HA without interpore connections), little bone formation was observed even in the surface pore areas.

## 6. BONE TISSUE ENGINEERING BY MESENCHYMAL STEM CELLS

The IP-CHA can be used as a scaffold for cell-based bone tissue engineering. We tested the efficacy of IP-CHA using a rat subcutaneous model by Ohgushi & Caplan (1999). Bone marrow cells were collected from the femur of rat and were cultivated in minimal essential medium supplemented with 15 per cent foetal bovine serum. IP-CHA discs ($R$=5 mm, $h$=2 mm) were soaked in the cell suspension overnight and further cultured in the same medium with β-glycerophosphate, ascorbic acid and dexamethasone for 14 days. The discs were then implanted into the subcutaneous tissue of rats and harvested for two to eight weeks after implantation. All the implants showed bone formation inside the pore areas as evidenced by decalcified histological sections and microcomputed tomography images (Nishikawa *et al.* 2004, 2005). At eight weeks after implantation, extensive bone volume was detected not only in the surface pore areas, but also in the centre pore areas of the implants (figure 7). The combination of IP-CHA and mesenchymal cells could be used as an excellent bone graft substitute because of its mechanical properties and capability of bone formation.

Recently, we have started a clinical trial with the combination of IP-CHA and autologous mesenchymal cells for bone tissue repair, and already treated 10 patients.

A precise clinical evaluation is necessary, but we believe that bone tissue engineering by IP-CHA offers new approaches to treatment for patients requiring skeletal reconstruction.

## 7. BONE TISSUE ENGINEERING BY BONE MORPHOGENETIC PROTEIN

Bone morphogenetic proteins (BMPs) are biologically active molecules capable of inducing new bone formation, and show potential for clinical use in bone defect repair

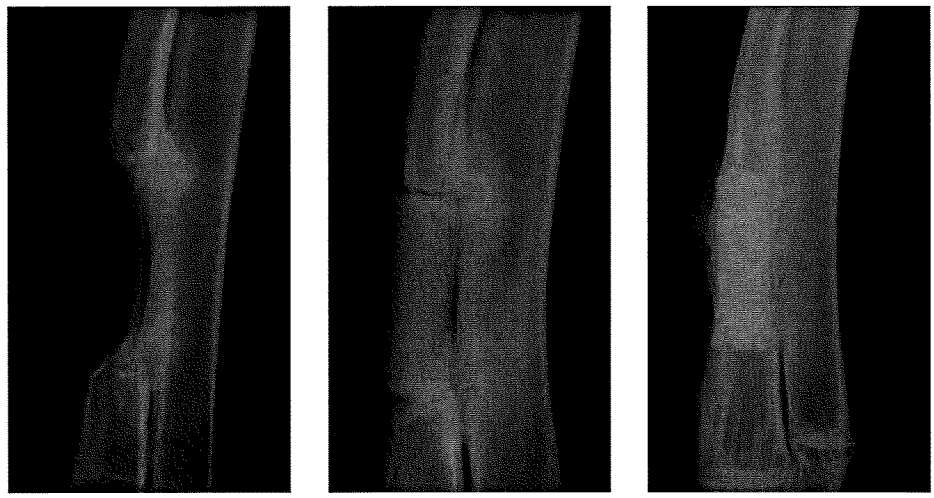

Figure 8. Bone healing by IP-CHA combined with BMP. (*a*) No implant group at eight weeks after surgery. No bone formation was detected. (*b*) IP-CHA group alone at eight weeks after implantation. Radiolucent lines were clearly visible between IP-CHA and host bone. (*c*) rhBMP-2 (5 μg)/IP-CHA group at eight weeks after implantation. Bony unions were observed at the junction sites and the radiodensity of IP-CHA increased.

(Wozney & Rosen 1998; Nakase & Yoshikawa 2006). However, an ideal system for delivering BMPs that can potentiate their bone-inducing ability and provide initial mechanical strength and scaffold for bone ingrowth has not yet been developed. We have analysed the efficacy of IP-CHA as a delivery system for recombinant human BMP-2 (rhBMP-2). We combined two biomaterials to construct a carrier/scaffold system for rhBMP-2: IP-CHA and a synthetic biodegradable polymer, poly-D,L-lactic acid–polyethyleneglycol block co-polymer (PLA-PEG; Miyamoto *et al.* 1993; Saito *et al.* 2001). A rabbit radius model was used to evaluate the bone-regenerating activity of the rhBMP-2/PLA-PEG/IP-CHA composite. All bone defects in groups treated with 5 μg of rhBMP-2 were completely fixed with sufficient strength at eight weeks after implantation (Kaito *et al.* 2005; figure 8). Using this carrier scaffold system, we reduced the amount of rhBMP-2 necessary for such results to approximately one-tenth of the amount needed in previous studies. Enhancement of bone formation is probably due to the superior osteoconduction ability of IP-CHA and the optimal drug delivery system provided by PLA-PEG. The PLA-PEG/IP-CHA composite is an excellent carrier/scaffold delivery system for rhBMP-2, and strongly encourages the clinical effects of rhBMP-2 in bone tissue regeneration.

## 8. BONE TISSUE ENGINEERING BY VASCULAR PREFABRICATION

Vascular network invasion into porous implants is another important aspect of using such materials as bone substitutes for large bone defects or in the construction of tissue-engineered bone, because cells cannot survive farther than a few hundred micrometres from a nutrient supply. The rate of new bone ingrowth into the porous material depends on vascular invasion from the surface of the implant, which is not fast enough in large implants to transport nutrients to cells transplanted in pores of the implant. Therefore, we examined whether prefabrication of IP-CHA with a vascular bundle enhances vascular network invasion into the pores via interpore connections (Akita *et al.* 2004; Myoui *et al.* 2004; Yoshikawa & Myoui 2005). When an IP-CHA cylindrical block was prefabricated with rat superficial inferior epigastric vessels, vascular invasion in the pores increased in both number and size, when compared with the control, resulting in more abundant fibrous connective tissue formation. Our findings suggest that inserting a vascular bundle into such interconnecting porous implants at the site of implantation supports vascular network invasion, which may eventually enhance bone ingrowth in the implants. Nakasa *et al.* (2005) reported that prefabrication of vascularized bone graft using a combination of fibroblast growth factor-2 and vascular bundle implantation into IP-CHA led to a satisfactory result in the reconstruction of bony defects.

## 9. APPLICATION FOR CARTILAGE REPAIR AND TENDON ATTACHMENT

We have developed a new technology for articular cartilage repair, consisting of a triple composite of rhBMP-2, PLA-PEG and IP-CHA, to induce the regeneration of both subchondral bone and articular cartilage (Tamai *et al.* 2005). Full-thickness cartilage defects in the rabbit were filled with the rhBMP-2 (20 μg)/PLA-PEG/IP-CHA composite. At six weeks, subchondral defects were completely repaired by subchondral bone and articular cartilage covering the bone. The regenerated cartilage manifested a hyaline-like appearance, with a columnar organization of chondrocytes and a mature matrix. The novel cell-free technology, the triple composite of rhBMP-2, PLA-PEG and IP-CHA, could mark a new development in the field of articular cartilage repair. Our new strategy for articular cartilage repair seems to be unique for the following three reasons: (i) we used autogenous mesenchymal cells efficiently recruited from bone

marrow by strongly activating the regeneration process of the subchondral bone defect, (ii) continuous BMP stimuli seemed to promote both the vigorous regeneration of subchondral bone and the following chondrocytic differentiation and cartilaginous matrix production at the surface resulting in hyaline-like cartilage regeneration in as little as three weeks, and (iii) the regenerated cartilage exhibited almost perfect lateral integration with the surrounding host cartilage, probably because the whole regeneration process in this system was *in situ* and efficient, unlike an *ex vivo* chondrocyte culture system. Ito *et al.* (2008) reported that an osteochondral plug using cultured chondrocytes and cylindrical IP-CHA plugs was successful in treating osteochondral defects in a rabbit model. Ohmae *et al.* have also tried to enhance tendon attachment to bone using IP-CHA with bone marrow stromal cells in a rabbit model, and obtained a satisfactory result (Omae *et al.* 2006, 2007).

## 10. CONCLUSIONS

The foam-gel technique is an innovative method that generates a three-dimensional fully interconnected porous structure in synthetic HA ceramics. The interconnected porous structure encourages bone ingrowth into the material and eventually leads to good incorporation of the material into the host bone. Our study indicated that IP-CHA exhibited excellent bone ingrowth in an animal model and favourable performance in clinical use. We believe that IP-CHA is an excellent bone substitute for filling bone defects and should be considered as an alternative to autogenous bone. In addition, IP-CHA seems likely to serve as a good scaffold for cell-based or cytokine-based tissue-engineered bone. In fact, we have been successful in bone tissue engineering using rhBMP-2, mesenchymal cells or vasculature in animals. The synthetic scaffold can be prefabricated into specific sizes and shapes to match bone defects, and even into a composite with the solid form of HA in order to reinforce its initial mechanical strength. IP-CHA is now commercially available in Japan, and we have applied IP-CHA as a bone substitute for the treatment of more than 80 patients with benign bone tumours or rheumatoid arthritis, and obtained some favourable clinical results. Recently, we have started a clinical trial with the combination of IP-CHA and autologous mesenchymal cells for bone tissue repair. Additional studies with larger animals including dogs or monkeys and precise clinical evaluation are necessary, but we believe that bone tissue engineering by IP-CHA offers new approaches to the treatment of patients requiring skeletal reconstruction.

The authors would like to thank Dr Kunio Takaoka for his invaluable advice regarding bone tissue engineering using rhBMP-2, and Dr Hajime Ohgushi for his invaluable advice regarding bone tissue engineering using bone marrow cells. We also thank Covalent Materials Corporation and MMT Co. Ltd for supplying materials. This work was supported in part by grants from the New Energy and Industrial Technology Development Organization (NEDO), the Ministry of Health, Labor and Welfare, Japan, and the Ministry of Education, Culture, Sports, Science and Technology, Japan.

## REFERENCES

Akita, S., Tamai, N., Myoui, A., Nishikawa, M., Kaito, T., Takaoka, K. & Yoshikawa, H. 2004 Capillary vessel network integration by inserting a vascular pedicle enhances bone formation in tissue-engineered bone using interconnected porous hydroxyapatite ceramics. *Tissue Eng.* **10**, 789–795. (doi:10.1089/1076327041348338)

Arrington, E. D., Smith, W. J., Chambers, H. G., Bucknell, A. L. & Davino, N. A. 1996 Complications of iliac crest bone graft harvesting. *Clin. Orthop.* **329**, 300–309. (doi:10.1097/00003086-199608000-00037)

Ayers, R. A., Simske, S. J., Nunes, C. R. & Wolford, L. M. 1998 Long-term bone ingrowth and residual micro hardness of porous block hydroxyapatite implants in humans. *J. Oral Maxillofac. Surg.* **56**, 1297–1301. (doi:10.1016/S0278-2391(98)90613-9)

Banwart, J. C., Asher, M. A. & Hassanein, R. S. 1995 Iliac crest bone graft harvest donor site morbidity. A statistical evaluation. *Spine* **20**, 1055–1060. (doi:10.1097/00007632-199505000-00012)

Bucholz, R. W., Carlton, A. & Holmes, R. E. 1987 Hydroxyapatite and tricalcium phosphate bone graft substitute. *Orthop. Clin. North Am.* **18**, 323–334.

Bucholz, R. W., Carlton, A. & Holmes, R. 1989 Interporous hydroxyapatite as a bone graft substitute in tibial plateau fractures. *Clin. Orthop.* **240**, 53–62.

Fujibayashi, S., Kim, H. M., Neo, M., Uchida, M., Kokubo, T. & Nakamura, T. 2003 Repair of segmental long bone defect in rabbit femur using bioactive titanium cylindrical mesh cage. *Biomaterials* **24**, 3445–3451. (doi:10.1016/S0142-9612(03)00221-7)

Holmes, R. E., Bucholz, R. W. & Mooney, V. 1987 Porous hydroxyapatite as a bone graft substitute in diaphyseal defects: a histometric study. *J. Orthop. Res.* **5**, 114–121. (doi:10.1002/jor.1100050114)

Holmes, R. E., Wardrop, R. W. & Wolford, L. M. 1988 Hydroxylapatite as a bone graft substitute in orthognathic surgery: histologic and histometric findings. *J. Oral Maxillofac. Surg.* **46**, 661–671. (doi:10.1016/0278-2391(88)90109-7)

Ito, Y., Adachi, N., Nakamae, A., Yanada, S. & Ochi, M. 2008 Transplantation of tissue-engineered osteochondral plug using cultured chondrocytes and interconnected porous calcium hydroxyapatite ceramic cylindrical plugs to treat osteochondral defects in a rabbit model. *Artif. Organs* **32**, 36–44.

Kaito, T., Myoui, A., Takaoka, K., Saito, N., Nishikawa, M., Tamai, N., Ohgushi, H. & Yoshikawa, H. 2005 Potentiation of the activity of bone morphogenetic protein-2 in bone regeneration by a PLA-PEG/hydroxyapatite composite. *Biomaterials* **26**, 73–79. (doi:10.1016/j.biomaterials.2004.02.010)

Kaito, T., Mukai, Y., Nishikawa, M., Ando, W., Yoshikawa, H. & Myoui, A. 2006 Dual hydroxyapatite composite with porous and solid parts: experimental study using canine lumbar interbody fusion model. *J. Biomed. Mater. Res. B* **78**, 378–384. (doi:10.1002/jbm.b.30498)

Martin, R. B., Chapman, M. W., Sharkey, N. A., Zissimos, S. L., Bay, B. & Shors, E. C. 1993 Bone ingrowth and mechanical properties of coralline hydroxyapatite 1 yr after implantation. *Biomaterials* **14**, 341–348. (doi:10.1016/0142-9612(93)90052-4)

Matsumine, A., Myoui, A., Kusuzaki, K., Araki, N., Seto, M., Yoshikawa, H. & Uchida, A. 2004 Calcium hydroxyapatite

ceramic implants in bone tumor surgery. A long-term follow-up study. *J. Bone Joint Surg. Br.* **86**, 719–725. (doi:10.1302/0301-620X.86B5.14242)

Miyamoto, S., Takaoka, K., Okada, T., Yoshikawa, H., Hashimoto, J., Suzuki, S. & Ono, K. 1993 Polylactic acid-polyethylene glycol block copolymer: a new biodegradable synthetic carrier for bone morphogenetic protein. *Clin. Orthop.* **294**, 333–343.

Myoui, A., Tamai, N., Nishikawa, M., Araki, N., Nakase, T., Akita, S. & Yoshikawa, H. 2004 Three-dimensionally engineered hydroxyapatite ceramics with interconnected pores as a bone substitute and tissue engineering scaffold. In *Biomaterials in orthopedics* (eds M. J. Yaszemski, D. J. Trantolo, K. U. Lewandrowski, V. Hasirci, D. E. Altobelli & D. L. Wise), pp. 287–300. New York, NY: Marcel Dekker.

Nakasa, T., Ishida, O., Sunagawa, T., Nakamae, A., Yasunaga, Y., Agung, M. & Ochi, M. 2005 Prefabrication of vascularized bone graft using a combination of fibroblast growth factor-2 and vascular bundle implantation into a novel interconnected porous calcium hydroxyapatite ceramic. *J. Biomed. Mater. Res.* **75A**, 350–355. (doi:10.1002/jbm.a.30435)

Nakase, T. & Yoshikawa, H. 2006 Potential roles of bone morphogenetic proteins (BMPs) in skeletal repair and regeneration. *J. Bone Mineral Metab.* **24**, 425–433. (doi:10.1007/s00774-006-0718-8)

Nishikawa, M. & Ohgushi, H. 2004 Calcium phosphate ceramics in Japan. In *Biomaterials in orthopedics* (eds M. J. Yaszemski, D. J. Trantolo, K. U. Lewandrowski, V. Hasirci, D. E. Altobelli & D. L. Wise), pp. 425–436. New York, NY: Marcel Dekker.

Nishikawa, M., Myoui, A., Ohgushi, H., Ikeuchi, M., Tamai, N. & Yoshikawa, H. 2004 Bone tissue engineering using novel interconnected porous hydroxyapatite ceramics combined with marrow mesenchymal cells: quantitative and three-dimensional image analysis. *Cell Transplant.* **13**, 367–376. (doi:10.3727/000000004783983819)

Nishikawa, M., Ohgushi, H., Tamai, N., Osuga, K., Uemura, M., Yoshikawa, H. & Myoui, A. 2005 The effect of simulated microgravity by three-dimensional clinostat on bone tissue engineering. *Cell Transplant.* **14**, 829–835. (doi:10.3727/000000005783982477)

Ohgushi, H. & Caplan, A. I. 1999 Stem cell technology and bioceramics: from cell to gene engineering. *J. Biomed. Mater. Res.* **48A**, 913–927. (doi:10.1002/(SICI)1097-4636(1999)48:6<913::AID-JBM22>3.0.CO;2-0)

Omae, H., Mochizuki, Y., Yokoya, S., Adachi, N. & Ochi, M. 2006 Effects of interconnecting porous structure of hydroxyapatite ceramics on interface between grafted tendon and ceramics. *J. Biomed. Mater. Res. A* **79**, 329–337. (doi:10.1002/jbm.a.30797)

Omae, H., Mochizuki, Y., Yokoya, S., Adachi, N. & Ochi, M. 2007 Augmentation of tendon attachment to porous ceramics by bone marrow stromal cells in a rabbit model. *Int. Orthop.* **31**, 353–358. (doi:10.1007/s00264-006-0194-8)

Prolo, D. J. & Rodrigo, J. J. 1985 Contemporary bone graft physiology and surgery. *Clin. Orthop.* **200**, 322–342. (doi:10.1097/00003086-198511000-00036)

Roy, T. D., Simon, J. L., Ricci, J. L., Rekow, E. D., Thompson, V. P. & Parsons, J. R. 2003 Performance of degradable composite bone repair products made via three-dimensional fabrication techniques. *J. Biomed. Mater. Res. A* **66**, 283–291. (doi:10.1002/jbm.a.10582)

Saito, N., Okada, T., Horiuchi, H., Murakami, N., Takahashi, J., Nawata, M., Ota, H., Miyamoto, S., Nozaki, K. & Takaoka, K. 2001 Biodegradable poly-D,L-lactic acid-polyethylene glycol block copolymers as a BMP delivery system for inducing bone. *J. Bone Joint Surg.* **83A**, S92–S98.

Sartoris, D. J., Gershuni, D. H., Akeson, W. H., Holmes, R. E. & Resnick, D. 1986 Coralline hydroxyapatite bone graft substitutes: preliminary report of radiographic evaluation. *Radiology* **159**, 133–137.

Shi, K., Hayashida, K., Hashimoto, J., Sugamoto, K., Kawai, H. & Yoshikawa, H. 2006 Hydroxyapatite augmentation for bone atrophy in total ankle replacement in rheumatoid arthritis. *J. Foot Ankle Surg.* **45**, 316–321. (doi:10.1053/j.jfas.2006.06.001)

Simon, J. L., Roy, T. D., Parsons, J. R., Rekow, E. D., Thompson, V. P., Kemnitzer, J. & Ricci, J. L. 2003 Engineered cellular response to scaffold architecture in a rabbit trephine defect. *J. Biomed. Mater. Res. A* **66**, 275–282. (doi:10.1002/jbm.a.10569)

Simon, J. L., Michna, S., Lewis, J. A., Rekow, E. D., Thompson, V. P., Smay, J. E., Yampolsky, A., Parsons, J. R. & Ricci, J. L. 2007 *In vivo* bone response to 3D periodic hydroxyapatite scaffolds assembled by direct ink writing. *J. Biomed. Mater. Res. A* **83**, 747–758. (doi:10.1002/jbm.a.31329)

Simon, J. L., Rekow, E. D., Thompson, V. P., Beam, H., Ricci, J. L. & Parsons, J. R. 2008 MicroCT analysis of hydroxyapatite bone repair scaffolds created via three-dimensional printing for evaluating the effects of scaffold architecture on bone ingrowth. *J. Biomed. Mater. Res. A* **85**, 371–377.

Steinkamp, J. A., Hansen, K. M. & Crissman, H. A. 1976 Flow microfluorometric and light-scatter measurement of nuclear and cytoplasmic size in mammalian cells. *J. Histochem. Cytochem.* **24**, 292–297.

Tamai, N., Myoui, A., Tomita, T., Nakase, T., Tanaka, J., Ochi, T. & Yoshikawa, H. 2002 Novel hydroxyapatite ceramics with an interconnective porous structure exhibit superior osteoconduction *in vivo*. *J. Biomed. Mater. Res.* **59A**, 110–117. (doi:10.1002/jbm.1222)

Tamai, N., Myoui, A., Hirao, M., Kaito, T., Ochi, T., Tanaka, J., Takaoka, K. & Yoshikawa, H. 2005 A new biotechnology for articular cartilage repair: subchondral implantation of a composite of interconnected porous hydroxyapatite, synthetic polymer (PLA/PEG), and bone morphogenetic protein-2 (rhBMP-2). *Osteoarthr. Cartil.* **13**, 405–417. (doi:10.1016/j.joca.2004.12.014)

Uchida, A., Nade, S. M., McCartney, E. R. & Ching, W. 1984 The use of ceramics for bone replacement. A comparative study of three different porous ceramics. *J. Bone Joint Surg. Br.* **66**, 269–275.

Uchida, A., Araki, N., Shinto, Y., Yoshikawa, H., Kurisaki, E. & Ono, K. 1990 The use of calcium hydroxyapatite ceramic in bone tumour surgery. *J. Bone Joint Surg. Br.* **72**, 298–302.

Wozney, J. M. & Rosen, V. 1998 Bone morphogenetic protein and bone morphogenetic protein gene family in bone formation and repair. *Clin. Orthop.* **346**, 26–37. (doi:10.1097/00003086-199801000-00006)

Yoshikawa, H. & Myoui, A. 2005 Bone tissue engineering with porous hydroxyapatite ceramics. *J. Artif. Organs* **8**, 131–136. (doi:10.1007/s10047-005-0292-1)

Yoshikawa, H. & Uchida, A. 1999 Clinical application of calcium hydroxyapatite ceramic in bone tumor surgery. In *Biomaterials and bioengineering handbook* (ed. D. L. Wise), pp. 433–455. New York, NY: Marcel Dekker.

# Three-Dimensional Kinematics of the Rheumatoid Wrist After Partial Arthrodesis

By Sayuri Arimitsu, MD, Tsuyoshi Murase, MD, PhD, Jun Hashimoto, MD, PhD, Hideki Yoshikawa, MD, PhD, Kazuomi Sugamoto, MD, PhD, and Hisao Moritomo, MD, PhD

*Investigation performed at the Department of Orthopaedic Surgery, Osaka University, Osaka, Japan*

**Background:** Partial arthrodesis of the wrist, such as radiolunate and radioscapholunate arthrodesis, is intuitively more appealing for the treatment of the rheumatoid wrist than total arthrodesis is because it preserves some motion. However, wrist kinematics after partial arthrodesis are incompletely understood. The purpose of the present study was to evaluate the kinematics of the radiocarpal and midcarpal joints of rheumatoid wrists with use of three-dimensional computed tomography before and after partial arthrodesis.

**Methods:** We selected ten wrists that were affected by rheumatoid arthritis in which the radiolunate joint was severely damaged but the midcarpal joint congruities were relatively well preserved. Six radiolunate and four radioscapholunate arthrodeses were then performed, with preservation of the joint congruity between the scaphoid, lunate, and capitate. We acquired in vivo three-dimensional kinematic data during wrist flexion-extension preoperatively and postoperatively with use of computed tomography and a markerless bone-registration technique. Postoperative midcarpal joint congruity and range of motion were compared with preoperative values.

**Results:** The mean range of global wrist motion was 48° ± 21° after radiolunate arthrodesis and 47° ± 14° after radioscapholunate arthrodesis. Midcarpal joint congruities and motion between the scaphoid, lunate, and capitate were well preserved in all ten wrists. The postoperative range of capitate motion relative to the lunate was 109% of the preoperative value after radiolunate arthrodesis and 88% after radioscapholunate arthrodesis. The directions of capitate motion relative to the lunate after both types of partial arthrodesis were significantly more oblique than before the arthrodeses, changing from radiodorsal to ulnopalmar along the so-called dart-throwing motion plane ($p < 0.05$).

**Conclusions:** The results of this kinematic analysis, which showed that midcarpal motion occurred in the dart-throwing motion plane, may support the use of radiolunate and radioscapholunate arthrodeses as an alternative to total wrist arthrodesis in patients with symptomatic rheumatoid arthritis of the wrist.

**Level of Evidence:** Therapeutic Level IV. See Instructions to Authors for a complete description of levels of evidence.

The aim of the surgical treatment of the wrist that is affected by rheumatoid arthritis is to achieve a painless, stable, and functional joint[1]. Total wrist arthrodesis has been used in severe cases in which there is collapse of both the radiocarpal and midcarpal articulations. A high fusion rate and good pain relief can be expected, but many patients find the loss of motion to be limiting[2]. In a painful wrist with destruction of the radiocarpal joint and an intact midcarpal joint, preservation of partial motion is a worthwhile goal[2]. Partial arthrodesis of the wrist, such as radiolunate or radioscapholunate arthrodesis, might be preferable. The choice between total and partial arthrodesis is usually decided on the basis of radiographs alone. However, a recent three-dimensional study revealed that the midcarpal motion of wrists with rheumatoid arthritis was better preserved than previously thought and suggested a more positive view of the utility of partial arthrodesis[3].

Radiolunate arthrodesis is a well-established procedure, and several researchers have reported successful clinical results in association with this operation[1,4-12]. It has been suggested that radiolunate arthrodesis is most useful for the treatment of

**Disclosure:** In support of their research for or preparation of this work, one or more of the authors received, in any one year, outside funding or grants of less than $10,000 from the Nakatani Foundation of Electronic Measuring Technology Advancement. Neither they nor a member of their immediate families received payments or other benefits or a commitment or agreement to provide such benefits from a commercial entity. No commercial entity paid or directed, or agreed to pay or direct, any benefits to any research fund, foundation, division, center, clinical practice, or other charitable or nonprofit organization with which the authors, or a member of their immediate families, are affiliated or associated.